Materials Chemistry and Physics 135 (2012) 810–817

Contents lists available at SciVerse ScienceDirect

Materials Chemistry and Physics

journal homepage: www.elsevier.com/locate/matchemphys

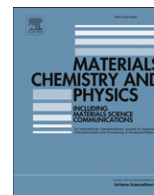

Morphology evolution of hydrothermally grown ZnO nanostructures on gallium doping and their defect structures

G. Pineda-Hernández [a], A. Escobedo-Morales [a,*], U. Pal [b], E. Chigo-Anota [a]

[a] Facultad de Ingeniería Química, Benemérita Universidad Autónoma de Puebla, C.P. 72570 Puebla, Pue., Mexico
[b] Instituto de Física, Benemérita Universidad Autónoma de Puebla, Apdo. Postal J-48, C.P. 72570 Puebla, Pue., Mexico

HIGHLIGHTS

► Ga doped ZnO nanostructures were successfully grown by hydrothermal chemical route.
► Ga doping has strong effect on the resulting morphology of ZnO nanostructures.
► Anomalous vibrational modes in wurtzite ZnO lattice are induced by Ga doping.
► Incorporated Ga atoms accommodate at preferential lattice sites.

ARTICLE INFO

Article history:
Received 28 April 2011
Received in revised form
18 April 2012
Accepted 20 May 2012

Keywords:
Semiconductors
Crystal growth
Defects
Phonons

ABSTRACT

In the present article, the effect of gallium doping on the morphology, structural, and vibrational properties of hydrothermally grown ZnO nanostructures has been studied. It has been observed that incorporated gallium plays an important role on the growth kinetics and hence on the morphology evolution of the ZnO crystals. Ga doping in high concentration results in the contraction of ZnO unit cell, mainly along *c*-axis. Although Ga has high solubility in ZnO, heavy doping promotes the segregation of Ga atoms as a secondary phase. Incorporated Ga atoms strongly affect the vibrational characteristics of ZnO lattice and induce anomalous Raman modes. Possible mechanisms of morphology evolution and origin of anomalous Raman modes in Ga doped ZnO nanostructures are discussed.

© 2012 Elsevier B.V. All rights reserved.

1. Introduction

Due to its wide direct band gap at room temperature (3.37 eV) and large exciton binding energy (60 meV), zinc oxide (ZnO) has been recognized among the most promising semiconductors to fabricate optoelectronics devices, like solar cells [1], gas sensors [2], field emitters [3], light emitting devices [4,5], and UV lasers [6], to name a few. Moreover, due to its chemical stability under oxidizing environments and biocompatibility, it is a useful material for applications in catalysis [7], medicine [8], and cosmetics [9]. It is well known that on tuning the chemical composition, morphology and size, the physical and chemical properties of ZnO can be controlled. Therefore, a huge effort has been devoted to obtain doped and undoped ZnO of different characteristics [10–16]. For example, when ZnO is doped with group III-A elements, such as Al or Ga, its electrical resistivity can be reduced as low as 10^{-4} Ω cm [17], making doped ZnO a candidate to replace indium tin oxide (ITO) as transparent conducting material. As Zn and Ga have similar atomic radii, Ga is highly soluble in ZnO; consequently gallium doping is a suitable alternative for controlling the optoelectronic properties of ZnO samples without compromising their crystallinity. In this regard, crystalline gallium zinc oxide (GZO) nanostructures have been obtained by thermal evaporation [18], spray pyrolysis [19], r.f. magnetron sputtering [20], pulsed laser deposition [21], molecular-beam epitaxy [22], metal–organic chemical vapor deposition [23], arc-discharge [24], hydrothermal process [25], sol–gel technique [26], among others. Nevertheless, extensive descriptions concerning the effect of optoelectronic doping on the morphology, structural and vibrational properties are scarce [27].

Apart from the adequate band gap and exciton energy, the efficiency of optoelectronic devices depends on their electronic characteristics like electron mobility and free carrier density. Although doping process commonly increases the free carrier concentration, high doping levels could introduce large amounts of electron scattering centers, reducing the electron mobility. Also, strong interaction of free carriers with lattice vibrations (phonons)

* Corresponding author. Tel.: +52 222 229 55 00x7250/7259.
E-mail address: alejandroescobedo@hotmail.com (A. Escobedo-Morales).

0254-0584/$ – see front matter © 2012 Elsevier B.V. All rights reserved.
doi:10.1016/j.matchemphys.2012.05.062

could reduce the electron mobility even further. Therefore, a thorough study of the structural and vibrational properties of doped materials is desired before their use in optoelectronic devices.

Here we present a detailed study of the effect of gallium doping concentration on the morphology, structural and vibrational properties of hydrothermally grown ZnO nanostructures.

2. Experimental section

The following chemicals were purchased and used as received without further purification: ethylenediamine [EDA, $NH_2(CH_2)_2NH_2$; J.T. Baker, 99.9%], zinc acetate dihydrate [$Zn(CH_3COO)_2 \cdot 2H_2O$; J.T. Baker, 99.99%], sodium hydroxide (NaOH; J.T. Baker, 99.99%), and gallium (III) nitrate hydrate [$Ga(NO_3)_3 \cdot xH_2O$; Aldrich, 99.99%]. In a typical synthesis process 45 ml of deionized water (18.0 MΩ cm) and 5 ml of EDA were mixed thoroughly under magnetic stirring. Then 4270.8 mg of zinc acetate was slowly dissolved in the previous solution. After that, about 708.3 mg of sodium hydroxide was added to the previous mixture to increase its pH to 12. Then the solution is heated up to 100 °C and maintained at this temperature for 15 h. Afterward it was cooled freely to room temperature. Finally, the obtained precipitate was filtered and washed with deionized water several times. For doped samples, specific amounts (12.5, 25.0, 50.3, 127.6, 261.9, and 552.9 mg) of the gallium salt were added to the previously described aqueous solution to prepare the samples with nominal 0.25, 0.50, 1.0, 2.50, 5.0, and 10.0% gallium doped samples. The following relation was used to calculate the amount of gallium salt used for each sample: $Ga\% = [M_{Ga}]/([M_{Ga}] + [M_{Zn}]) \times 100\%$, where Ga% is the nominal gallium doping, and $[M_{Ga}]$ and $[M_{Zn}]$ are the molar concentration of Ga and Zn in the aqueous solution, respectively.

All the samples were analyzed by scanning electron microscopy/energy dispersive X-ray spectroscopy (SEM/EDS; Jeol JSM 6610LV), transmission electron microscopy (TEM; Philips Tecnai F20 TEM), X-ray diffraction (XRD; Bruker Advance D8, CuK_α, $\lambda = 1.5406$ Å), and room temperature Raman spectroscopy in backscattering configuration using the 633 nm line of a He–Ne laser as excitation source (LabRAM HR-Olympus Micro Raman system).

3. Results and discussion

Fig. 1 shows the typical SEM images of undoped and doped samples. It can be noted that the gallium doping has a strong effect on the resulting morphology of the ZnO structures. As the gallium content increases, the morphology progressively turns from urchin-like (undoped) to rose-like structures (10.0% Ga doped). Also it is evident that the morphology of the crystalline units which constitute the urchin-like structures is not the same for all the samples. For the undoped sample, the units have needle-like morphology with average diameter of 200 nm and about 6 microns length. However, as the concentration of gallium content increases, fewer, but thicker crystalline units are obtained with crystal habit resembling hexagonal prisms (see Fig. 1e and f). In addition, it is interesting to note that as the gallium content increases, the tip of these nanostructures gradually turns from smooth to rough surfaces (marked with rectangles in Fig. 1). In order to obtain additional information of this peculiar feature, HAADF and elemental mapping images of the 5.0% nominal Ga doped sample were acquired (Fig. 2). As can be seen, a homogeneous distribution of Zn, O and Ga is observed along the body of the rods. However, an increase of Ga content is recognized (Fig. 2d) at the tip of the nanostructures, probably due to a depletion of available ZnO growth units as the growth process advances. These

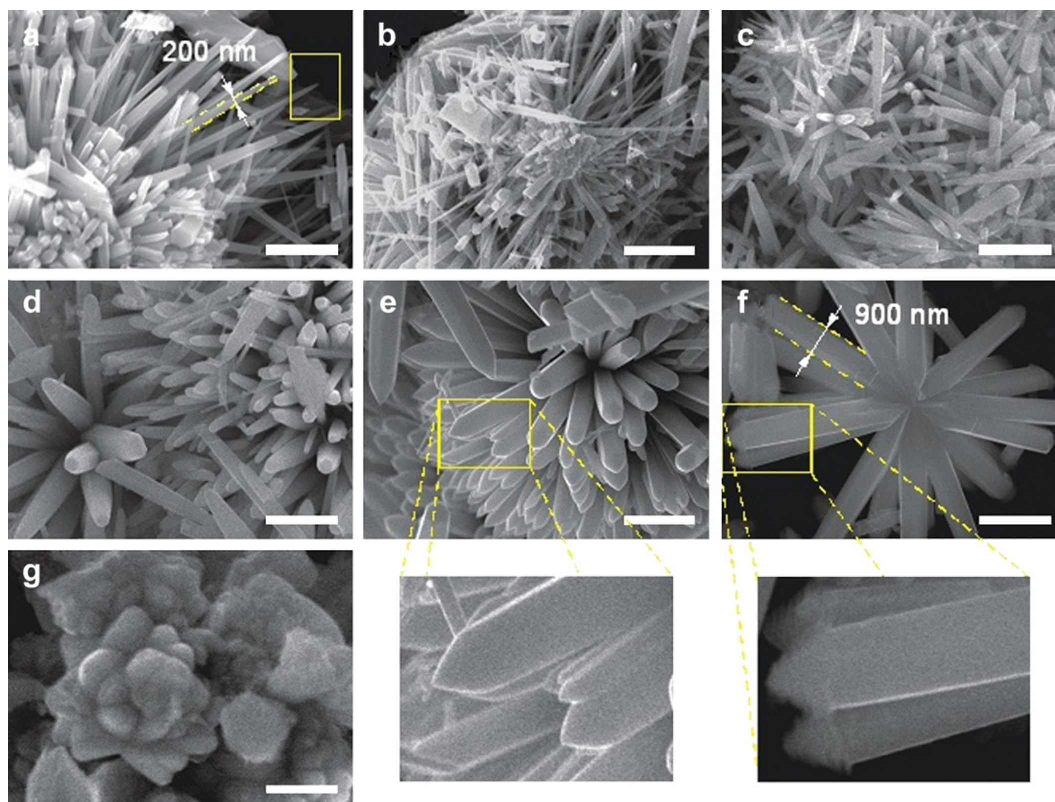

Fig. 1. Typical SEM images of undoped (a), 0.25 (b), 0.50 (c), 1.0 (d), 2.50 (e), 5.0 (f), and 10.0% (g) nominal Ga doped samples. All the scale bars correspond to 2 microns.

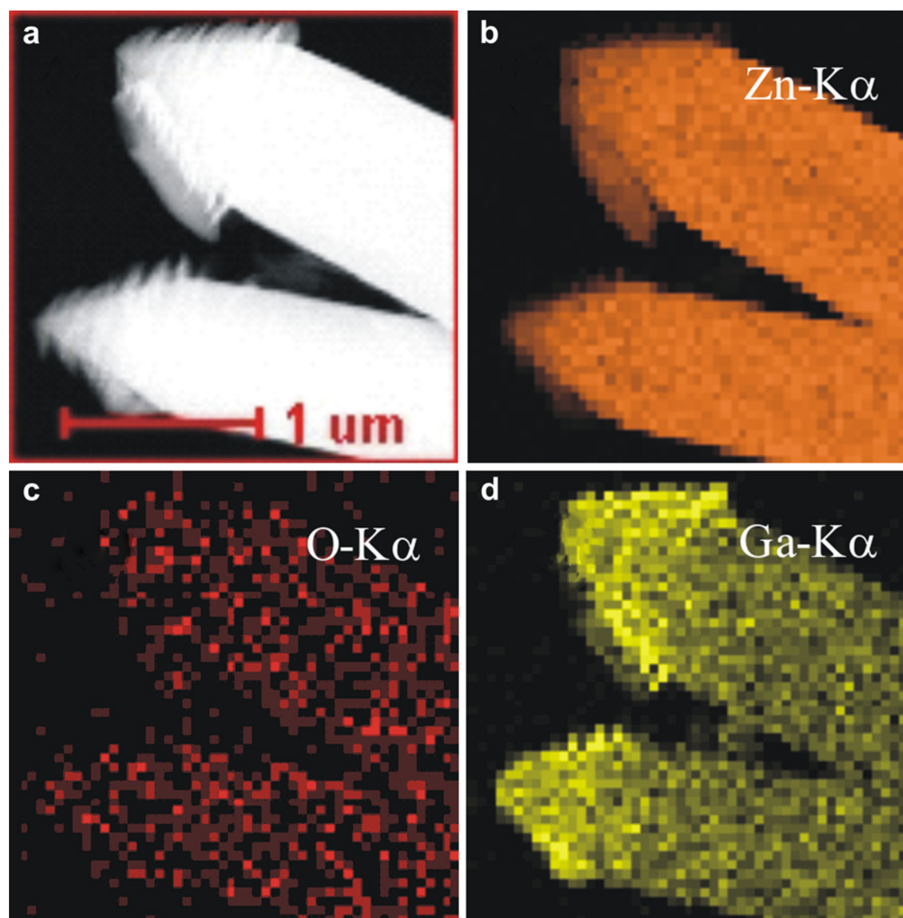

Fig. 2. HAADF image (a), and EDS elemental maps (b–d) of 5.0% nominal Ga doped ZnO nanorods.

rough structures, along with the observed rose-like morphology of the heaviest doped sample indicate that a large Ga content in the reaction mixture modifies the growth mechanism, resulting the observed morphology. In this regard, Goh et al. [28] have found that structural defects effectively can drive the growth mechanism of hydrothermally grown crystals.

The overall composition of doped and undoped ZnO nanostructures was analyzed by EDS. The obtained results are summarized in Table 1. It can be noted that the Ga atomic percent (at.%) does not follow a linear relationship with the nominal Ga doping concentration; instead, a nearly exponential relationship was recognized. Elemental composition of samples suggests that gallium is incorporated into the ZnO lattice mainly as substitutional impurity. Since the Ga has an extra valence electron ($4s^2\,4p^1$) than Zn ($4s^2$), presence of Ga_{Zn} defects in high quantity must increase the charge carrier density and the conductivity of ZnO crystals. However, at the same time, new electron scattering centers are produced and the electron mobility could be compromised. Electrical measurements of the undoped and doped samples are in progress to verify these effects.

Table 1
Elemental composition of undoped and Ga doped ZnO samples.

Nominal Ga doping (%)	At.% (EDS average)		
	Zn	O	Ga
0.00	47.73	52.27	0.00
0.25	48.39	51.55	0.06
0.50	52.50	47.42	0.08
1.00	46.90	52.95	0.15
2.50	50.16	49.55	0.29
5.00	40.44	58.47	1.08
10.00	41.20	53.95	4.85

XRD patterns of the undoped and gallium doped samples are presented in Fig. 3. For the undoped sample, all the diffraction peaks match with those reported for ZnO in wurtzite phase (*w*-ZnO) [29]; no additional diffraction peaks were found. Since similar XRD patterns are also observed for the doped samples, it is inferred that Ga doping does not affect structural phase (hexagonal) of ZnO. However, a detailed inspection of the XRD pattern of the heaviest doped sample (10.0%) reveals three tiny reflections located at about 33.56, 35.28, and 59.32° (see supporting information). These reflections could not be related to *w*-ZnO phase, instead they were attributed to β-Ga_2O_3 traces (monoclinic) [30]. It is worth to note that the intensity of the diffraction peaks assigned to *w*-ZnO does not decease noticeably on increasing the gallium content in the samples, which suggests that incorporation of Ga atoms into the ZnO lattice does not introduce considerable lattice deformation. Since the ionic radii of Zn^{2+} (0.74 Å) and Ga^{3+} (0.62 Å) are similar, large distortion of ZnO lattice due to gallium doping is not expected. Fig. 4 shows the variation of the position of the main diffraction peaks of the ZnO nanostructures with the concentration of nominal Ga doping. It was observed that except for the heaviest doped sample, the positions of the (100), (002), and (101) diffraction peaks remain almost fixed. For the heaviest doped sample, these diffraction peaks shift to higher angles, indicating that the ZnO lattice parameters are shortened. Similar behavior has been previously observed in GZO thin films [31,32]. It is worth to note that while the (100) peak is shifted by around 0.04°, the (002) peak shifted about 0.17°. It follows that the

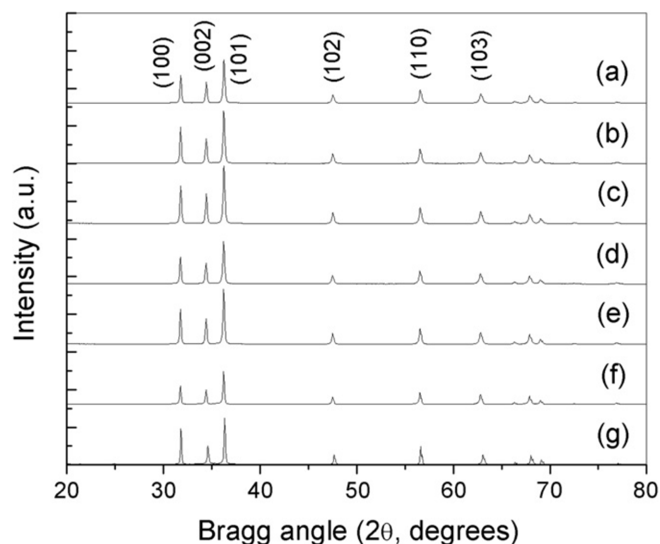

Fig. 3. Powder X-ray diffraction patterns of undoped (a), 0.25 (b), 0.50 (c), 1.0 (d), 2.50 (e), 5.0 (f), and 10.0% (g) nominal Ga doped samples. Miller indices of the main diffraction peaks related to *w*-ZnO phase are indicated for undoped sample.

main lattice distortion is along the *c* rather than *a* axis. In Table 2 the position and full width at half maximum (FWHM) of the main diffraction peaks, along with the calculated lattice parameter values for the undoped and gallium doped samples are summarized. The lattice parameters were calculated through the least square fit procedure described by Giacovazzo et al. [33]. It is worth to note that although the resulting morphologies of the undoped and 10.0% Ga doped samples differ considerably, their crystal qualities are quite similar, as the relative intensity and FWHM of their diffraction peaks suggests. Therefore, it is proposed that while the incorporation of Ga strongly affects the crystal growth kinetics and surface energy of the crystalline planes, it does not have any strong influence on the crystalline quality of ZnO nanostructures.

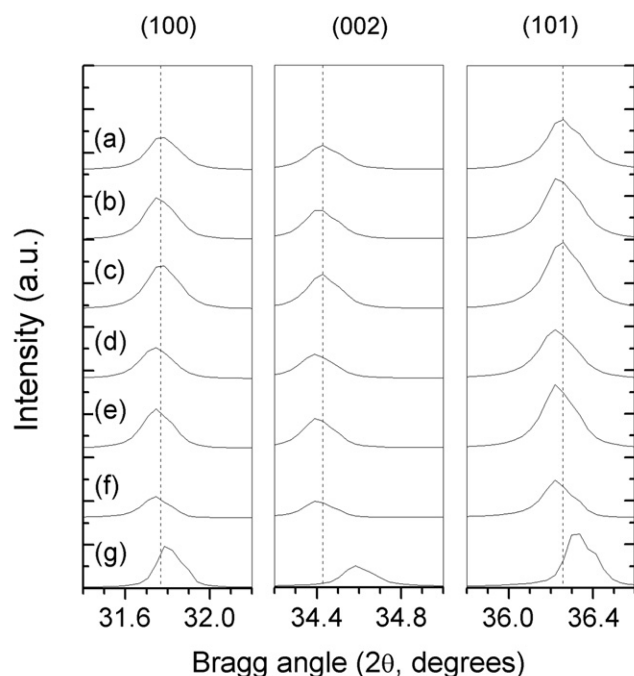

Fig. 4. Evolution of the (100), (002) and (101) diffraction peaks in the undoped (a), 0.25 (b), 0.50 (c), 1.0 (d), 2.50 (e), 5.0 (f), and 10.0% (g) nominal Ga doped ZnO sample.

Table 2
Position and full width at half maximum (FWHM) of the main diffraction peaks of undoped and doped samples along with their calculated lattice parameters *a* and *c*.

Nominal Ga doping (%)	Position and FWHM (degrees)			Lattice parameter (Å)		
	(100)	(002)	(101)	*a*	*c*	*c*/*a*
0.00	31.77(9) 0.17(9)	34.43(3) 0.19(2)	36.26(2) 0.21(7)	3.24(9)	5.20(6)	1.60(2)
0.25	31.76(4) 0.17(9)	34.42(0) 0.19(1)	36.24(8) 0.21(3)	3.25(0)	5.20(6)	1.60(1)
0.50	31.77(5) 0.18(7)	34.42(9) 0.18(8)	36.25(9) 0.21(6)	3.24(9)	5.20(6)	1.60(2)
1.0	31.74(3) 0.18(3)	34.39(7) 0.19(5)	36.22(6) 0.21(2)	3.25(1)	5.20(9)	1.60(2)
2.50	31.75(0) 0.17(3)	34.40(6) 0.18(4)	36.23(5) 0.19(7)	3.25(1)	5.20(8)	1.60(1)
5.0	31.73(8) 0.15(7)	34.40(2) 0.16(8)	36.22(0) 0.17(1)	3.25(3)	5.21(0)	1.60(1)
10.0	31.81(0) 0.14(6)	34.60(0) 0.17(7)	36.33(7) 0.16(8)	3.24(7)	5.18(3)	1.59(6)

The wurtzite ZnO structure belongs to the $P6_3mc$ space group. Its crystal structure can be described as a successive stacking of Zn and O monoatomic layers along the fundamental *c* lattice vector. Because of the large difference in electronegativities between zinc (2.2) and oxygen (3.6) [34], their interatomic bonding has a strong polar character. Such feature produces a net dipolar moment. The dipole moment and the lack of an inversion center are the origin of the well known piezoelectric behavior of *w*-ZnO crystals. The natural habit of a ZnO crystal grown under quasi-equilibrium thermodynamic conditions looks like a hexagonal prism [35], where the top and bottom faces correspond to the polar lattice planes (001) and $(00\bar{1})$ consisting Zn- and O-terminated surfaces, respectively. The lateral crystallographic faces are parallel to the six-fold *c* axis, and they are disposed in the way to form 120° angle between adjacent faces. These lateral surfaces correspond to the non-polar {010} lattice planes [35]. The elongated morphology commonly observed for hydrothermally grown ZnO crystals is attributed to the large difference between the surface energy of non-polar and polar lattice planes [36,37]; it follows that, on modifying the surface energy of the different lattice planes, by either chemical adsorption of terminal species or incorporating defects [38,39], the resulting morphology might be controlled. For the present case, EDA was used as chelating agent and to support the elongated morphology induced by a fast growth along the [001] direction.

The chemical reactions involved in the growth process of the ZnO nanostructures are proposed as follows:

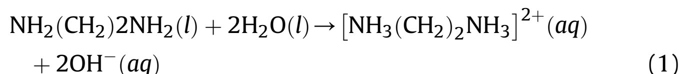

$$NH_2(CH_2)2NH_2(l) + 2H_2O(l) \rightarrow [NH_3(CH_2)_2NH_3]^{2+}(aq) + 2OH^-(aq) \quad (1)$$

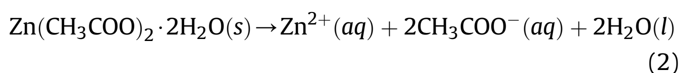

$$Zn(CH_3COO)_2 \cdot 2H_2O(s) \rightarrow Zn^{2+}(aq) + 2CH_3COO^-(aq) + 2H_2O(l) \quad (2)$$

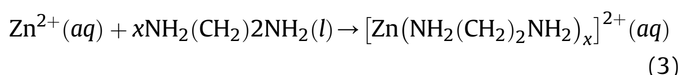

$$Zn^{2+}(aq) + xNH_2(CH_2)2NH_2(l) \rightarrow [Zn(NH_2(CH_2)_2NH_2)_x]^{2+}(aq) \quad (3)$$

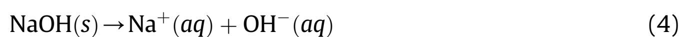

$$NaOH(s) \rightarrow Na^+(aq) + OH^-(aq) \quad (4)$$

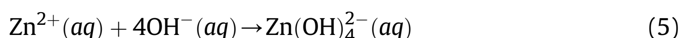

$$Zn^{2+}(aq) + 4OH^-(aq) \rightarrow Zn(OH)_4^{2-}(aq) \quad (5)$$

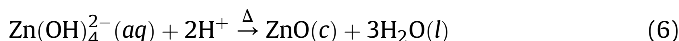

$$Zn(OH)_4^{2-}(aq) + 2H^+ \xrightarrow{\Delta} ZnO(c) + 3H_2O(l) \quad (6)$$

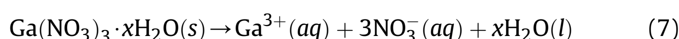

$$Ga(NO_3)_3 \cdot xH_2O(s) \rightarrow Ga^{3+}(aq) + 3NO_3^-(aq) + xH_2O(l) \quad (7)$$

Eq (1) states the formation of an alkaline solution (pH $\approx$ 11) as a result of the hydrolysis of EDA, a weak Lewis base, when it is dissolved in water. Once Zn^{2+} ions are introduced in the aqueous solution by the chemical dissociation of zinc acetate (Eq (2)), they are complexed by EDA (Eq (3)), which is a strong bidentate chelating agent [40]. The formation of analogous Zn–ammonium complexes in aqueous solutions with similar pH has been reported previously by Richardson and Lange [41]. However, on increasing the pH further by adding NaOH (Eq (4)), the amine molecules compete with hydroxyl groups to get bonded with Zn^{2+} ions (Eq (5)), until $Zn(OH)_4^{2-}$ becomes the predominant specie [42,43]. Gradually, as the temperature of the reaction mixture is increased a supersaturation state of zinc hydroxide is reached, leading to the formation of ZnO nuclei (Eq (6)). Under this scheme, it is expected that Ga ions (Eq (7)) have similar chemical behavior to Zn ions in the present alkaline solution.

The proposed growth stages of the undoped and gallium doped ZnO nanostructures are schematically shown in Fig. 5. Once the proper hydrothermal conditions are reached, nucleation process and subsequent formation of ZnO nuclei begin. At this stage the ZnO nuclei do not show preferential growth direction. When the density of ZnO nuclei is large enough, they begin to agglomerate [44]. Since the pH of the nutrient solution is well above of the isoelectric point for ZnO (pH $\sim$ 9.5) [45], the surface of the ZnO particles trends to charge negatively, mostly by adsorption of hydroxyl groups [38]. Later, as the individual ZnO crystals continue to grow, the polar character of wurtzite structure becomes evident [46]. As a result, the capping species (EDA:$2H^+$) are adsorbed mainly on the {010} planes. Although, adsorbed EDA:$2H^+$ facilitates an elongated morphology, a fast growth rate along the [001] direction due to the adsorption of $Zn(OH)_4^{2-}$ growth units in the positive Zn-terminated plane is the main reason of the resulting needle-like morphology [47].

It was observed that the incorporation of Ga salts retards the precipitation of ZnO and also reduces the reaction yield; therefore, the density of ZnO nuclei in the undoped sample must be higher than that for the doped samples. Lower density of ZnO nuclei results in fewer ZnO structures of bigger dimensions (see Fig. 1). This is because the growth process dominates over nucleation. A decrease of the density of ZnO nuclei due to Ga incorporation can be explained in terms of the classical nucleation model, which states that the driving force for a phase transition from solvated molecular precursors to a solid material is a change in the Gibbs free energy of the system (ΔG). This change depends on the growing particle radius (r), and consists of two contributions: first, the volume free energy, (ΔG_v), associated to the change in the free energy due to the phase transition from solvated precursors to a solid phase and second, the surface energy, (γ), the energy introduced to the system due to the formation of an interface [38]:

$$\Delta G = \frac{4}{3}\pi r^3 \Delta G_v + 4\pi r^2 \gamma \tag{8}$$

The addition of volume and surface terms in Eq (8) implies the formation of an energy barrier (ΔG^*), which must be overcome in order to obtain a nucleus of critical radius (r^*), beyond which it becomes stable and continues growing. The critical nucleus radius and the energy barrier are expressed as:

$$r^* = -\frac{2\gamma}{\Delta G_v} \tag{9}$$

$$\Delta G^* = \frac{16\pi\gamma^3}{3(\Delta G_v)^2} \tag{10}$$

We propose that the incorporation of gallium atoms into the ZnO lattice leads a decrease in ΔG_v, as certain amount of energy is

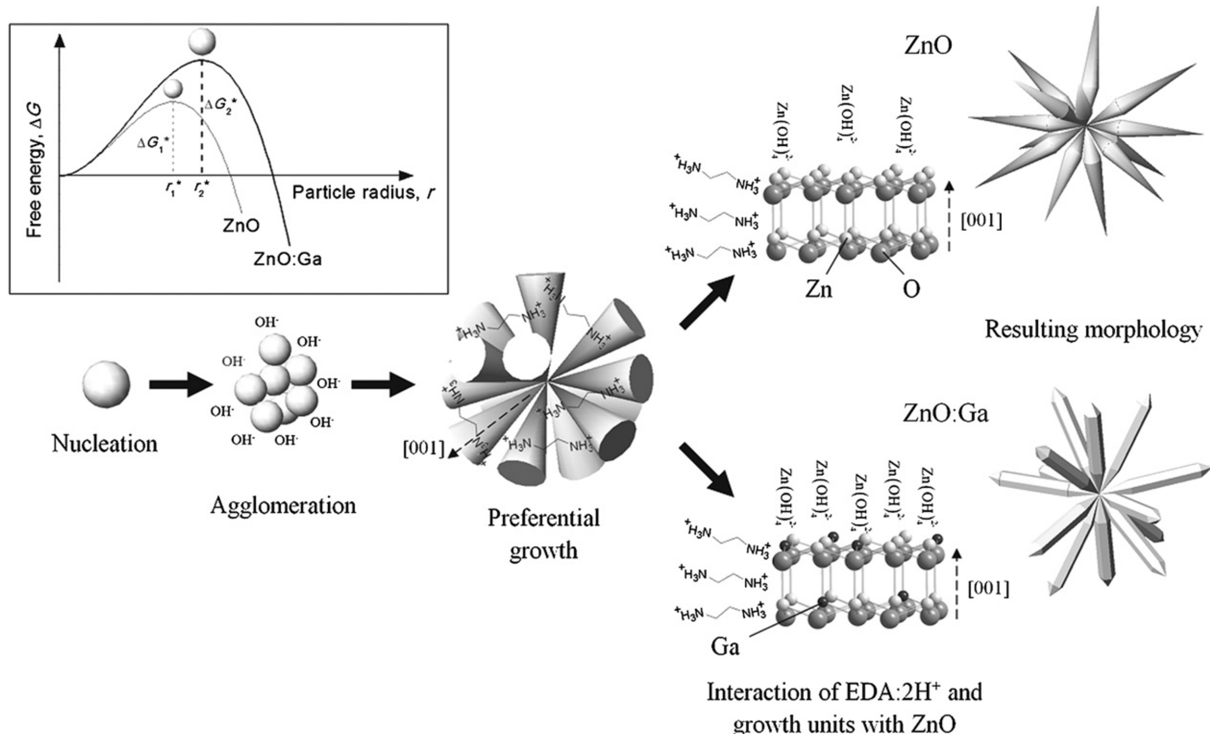

Fig. 5. Schematic presentation of the proposed growth stages for the undoped and doped ZnO nanostructures. The inset shows a schematic illustration of the effect of gallium doping on the free energy (ΔG), energy barrier (ΔG^*), and critical nucleus radius (r^*).

required to generate crystal defects. As can be seen from Eqs (9) and (10), a reduction of ΔG_v increases both the energy barrier to form a stable nucleus and its critical radius (see inset in Fig. 5), making doped crystallites more soluble than their undoped counterparts [48,49]; *i.e.*, the nucleation process is inhibited. The higher energy required to obtain stable doped ZnO nuclei can explain the experimental observation that the translucent aqueous solution turns opaque at higher temperatures as Ga molar concentration is increased. On the other hand, the formation of larger stable nuclei must occur at the expense their numbers, as they demand larger amounts of precursor species. The lower nuclei density allows the growth process to dominate over nucleation. Finally, it is inferred that high doping concentration (10.0%) leads to considerable change of the relative surface energy among the different lattice planes, inhibiting any preferential growth, and the characteristic hexagonal habit of *w*-ZnO crystals cannot be obtained.

Since the vibrational and structural properties of solids are closely related, a study of the effect of gallium doping on the vibrational properties of ZnO was performed. The irreducible relation of phononic modes at the center of Brillouin zone for *w*-ZnO structure, with four atoms per primitive cell, is stated by the relation: $\Gamma = 1A_1 + 2B_1 + 1E_1 + 2E_2$ [50], where A_1 and E_1 represent polar optical branches, which in turn split into longitudinal (LO) and transversal (TO) components. The two non-polar E_2 modes are related to the vibration of zinc (E_{2L}) and oxygen sub-lattices (E_{2H}). While A_1 and E_1 modes are Raman and infrared active, the E_2 modes are only active in Raman spectroscopy. On the other hand B_1 modes are inactive in both spectroscopies, and therefore they are called silent modes. It has been reported that breakdown of translational symmetry could relax the Raman selection rules, and as a consequence the B_1 modes could become active [51].

Fig. 6 presents the Raman spectrum of the undoped ZnO sample. The spectrum matches with that reported previously for wurtzite zinc oxide [52,53]; no additional Raman peaks associated to chemical reactants or possible sub-products were detected. The Raman signals located at about 101, 380, 411, 440, and 579 cm^{-1} were attributed to the first order E_{2L}, A_{1T}, E_{1T}, E_{2H} and LO modes, respectively. On the other hand, the peaks at around 204, 334 and 667 cm^{-1} were assigned to the 2-E_{2L}, E_{2H}–E_{2L} and 2-(E_{2H}–E_{2L}) second order modes, respectively [54]. In Fig. 7, the Raman spectra of undoped and gallium doped samples are shown for comparison. First, it can be noted that the Raman peaks associated

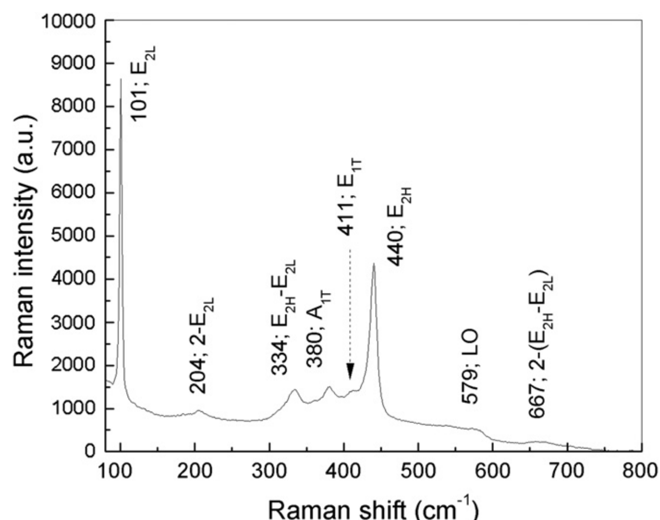

Fig. 6. Raman spectrum of the undoped ZnO sample.

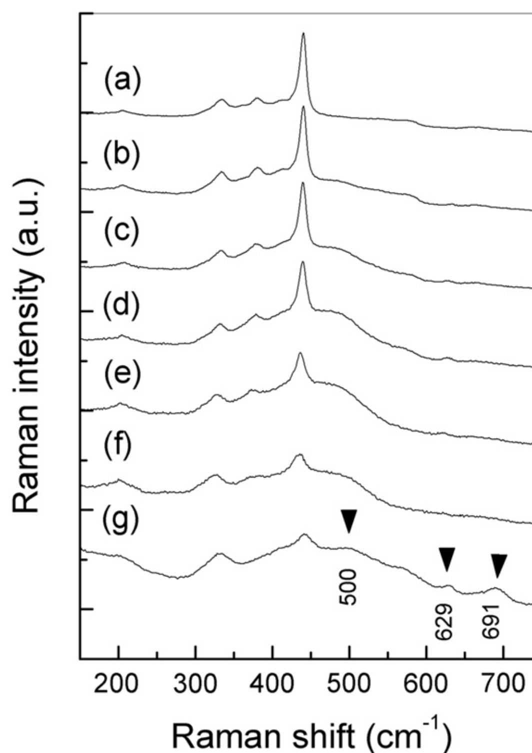

Fig. 7. Raman spectra of undoped (a), 0.25 (b), 0.50 (c), 1.0 (d), 2.50 (e), 5.0 (f), and 10.0% (g) nominal Ga doped samples. Anomalous Raman modes are pointed with arrows. For comparison, all the spectra were normalized respect to the intensity of the E_{2L} peak.

to *w*-ZnO phase get smaller and broader as gallium content increases, suggesting that the incorporation of Ga atoms induces lattice disorder. Second, gallium doping introduces three additional Raman peaks located at about 500, 629 and 691 cm^{-1}, and their intensities depend on Ga content. None of them could be assigned to some local vibrational mode (LVM's) using the effective masses relation [55]. Although the peak centered at 629 cm^{-1} could be assigned to A_g mode of β-Ga_2O_3 phase, it was attributed to a vibrational mode involving a gallium point defect, because the characteristic Raman spectrum of β-Ga_2O_3 shows two peaks located at 650 and 765 cm^{-1} [56–58], which were not observed for our doped samples. Observation of vibrational modes with similar frequencies (~631 cm^{-1}) have been reported to single phase ZnO:Ga samples [12]. The broad width of the Raman peak centered at 500 cm^{-1} suggests that its origin is not due to some particular point defect; instead it can be related to some complex defects involving either host or extrinsic atoms. Bundesmann et al. [12] have reported additional Raman modes in their Fe, Sb, Al, Ga and N doped ZnO thin films; all of them with frequencies around 510 cm^{-1}. Finally, to the best of our knowledge the peak at 691 cm^{-1} has not been previously reported for Ga doped ZnO samples. We propose that its origin involves specific point defects related to incorporated gallium atoms, probably Ga_{Zn} or Ga_i.

Fig. 8 shows the dependence of E_{2L} and E_{2H} Raman peaks with Ga content. It was found that while the frequency of these modes do not show clear dependence with Ga doping concentration, their shape are strongly affected as Ga concentration increases, specifically for the peak related to the oxygen sub-lattice (E_{2H}). As the atomic weight of Zn and Ga are close enough, incorporation of substitutional gallium atoms (Ga_{Zn}) affecting the features of the phononic mode associated to zinc sub-lattice (E_{2L}) substantially is not expected. On the other hand, since the main difference between

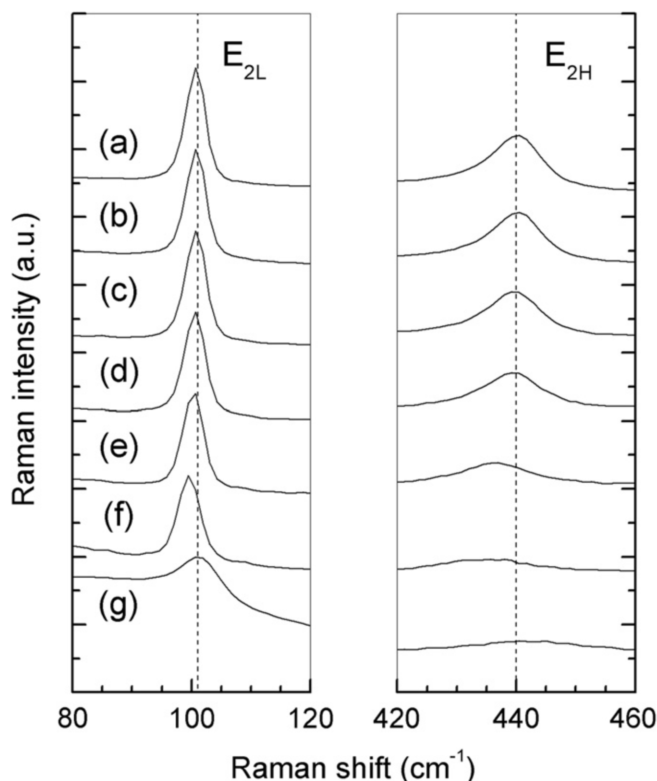

Fig. 8. Evolution of E_{2L} and E_{2H} Raman peaks on Ga doping: undoped (a), 0.25 (b), 0.50 (c), 1.0 (d), 2.50 (e), 5.0 (f), and 10.0% (g) nominal Ga doped sample.

Zn and Ga atoms resides on their valence electron configurations, and thus how they get bonded, it is proposed that the substitutional gallium atoms force the surrounding oxygen atoms to approach in, modifying their relative position and bond strength. As a consequence, the vibrational characteristics of the oxygen sub-lattice might substantially alter. The phenomenon can also explain a small contraction of the ZnO unit cell experimented for the heaviest Ga doped sample.

4. Conclusions

In summary, ZnO nanostructures with varied Ga concentrations were successfully grown by hydrothermal chemical route. The resulting morphology of the synthesized nanostructures has strong dependence on doping concentration, attributed to a competition between nucleation and growth process driven by Ga content. Although the unit cell of *w*-ZnO gets distorted a little bit on gallium doping along its *c* axis, incorporated Ga atoms accommodate at preferential lattice sites, indicating the feasibility to obtain solid solutions of Ga and ZnO. Ga doping in ZnO activates three anomalous Raman modes with frequencies of 500, 629 and 691 cm^{-1}. While the first mode is attributed to complex defects involving either native or extrinsic defects, the others two are related to point defects involving gallium atoms. The described hydrothermal method represents a low-cost alternative to obtain elongated nanostructures with controlled chemical composition which might be applied to fabricate light and field emitting devices.

Acknowledgments

We thank Carla de la Cerna and Ricardo A. Serrano (CUV-BUAP) for their assistance to acquire the SEM micrographs and XRD patterns of the nanostructures. This work was partially supported by the Mexican Council of Science and Technology (Grants # CONACyT CB-168027 & CONACyT CB-151767) and VIEP-BUAP.

Appendix A. Supplementary material

Supplementary material associated with this article can be found, in the online version, at doi:10.1016/j.matchemphys.2012.05.062.

References

[1] J.B. Baxter, E.S. Aydil, Appl. Phys. Lett. 86 (2005) 053114.
[2] J. Zhang, Sh. Wang, M. Xu, Y. Wang, B. Zhu, Sh. Zhang, W. Huang, Sh. Wu, Cryst. Growth Des. 9 (2009) 3532.
[3] C.X. Xu, X.W. Sun, B.J. Chen, Appl. Phys. Lett. 84 (2004) 1540.
[4] H.J. Bolink, E. Coronado, M. Sessolo, Chem. Mater. 21 (2009) 439.
[5] H.Q. Le, S.K. Lim, G.K.L. Goh, S.J. Chua, N.S.S. Ang, W. Liu, Appl. Phys. B 100 (2010) 705.
[6] H.K. Liang, S.F. Yu, H.Y. Yang, Appl. Phys. Lett. 96 (2010) 101116.
[7] D. Chu, Y. Masuda, T. Ohji, K. Kato, Langmuir 24 (2010) 2811.
[8] Y.-E. Choi, J.-W. Kwak, J.W. Park, Sensors 10 (2010) 428.
[9] Ch.-L. Kuo, Ch.-L. Wang, H.-H. Ko, W.-S. Hwang, K.-M. Chang, W.-L. Li, H.-H. Huang, Y.-H. Chang, M.-Ch. Wang, Ceram. Int. 36 (2010) 693.
[10] X. Wang, Sh. Yang, J. Wang, M. Li, X. Jiang, G. Du, X. Liu, R.P.H. Chang, J. Cryst. Growth 226 (2001) 123.
[11] K. Ueda, H. Tabata, T. Kawai, Appl. Phys. Lett. 79 (2001) 988.
[12] C. Bundesmann, N. Ashkenov, M. Schubert, D. Spemann, T. Butz, E.M. Kaidashev, M. Lorenz, M. Grundmann, Appl. Phys. Lett. 83 (2003) 1974.
[13] F.X. Xiu, Z. Yang, L.J. Mandalapu, D.T. Zhao, J.L. Liu, W.P. Beyermann, Appl. Phys. Lett. 87 (2005) 152101.
[14] A. Escobedo-Morales, M. Herrera Zaldivar, U. Pal, Opt. Mater. 29 (2006) 100.
[15] H.Q. Le, S.K. Lim, G.K.L. Goh, J. Cryst. Growth 312 (2010) 437.
[16] G.K. Lau, T.S. Zhang, G.K.L. Goh, J. Nanosci, Nanotechnol. 10 (2010) 4733.
[17] M. Yan, H.T. Zhang, E.J. Widjaja, R.P.H. Chang, J. Appl. Phys. 94 (2003) 5240.
[18] L.W. Chang, J.W. Yeh, C.L. Cheng, F.S. Shieu, H.C. Shih, Appl. Surf. Sci. 257 (2011) 3145.
[19] T.P. Rao, M.C.S. Kumar, J. Alloys Compd. 506 (2010) 788.
[20] J.-Y. Tseng, Y.-T. Chen, M.-Y. Yang, Ch.-Y. Wang, P.-Ch. Li, W.-Ch. Yu, Y.F. Hsu, S.F. Wang, Thin Solid Films 517 (2009) 6310.
[21] S.-M. Park, T. Ikegami, K. Ebihara, Thin Solid Films 513 (2006) 90.
[22] Z. Yang, D.C. Look, J.L. Liu, Appl. Phys. Lett. 94 (2009) 072101.
[23] H. Chen, A. Du Pasquier, G. Saraf, J. Zhong, Y. Lu, Semicond. Sci. Technol. 23 (2008) 045004.
[24] G.-S. Park, W.-B. Choi, J.-M. Kim, Y.Ch. Choi, Y.H. Lee, Ch.-B. Lim, J. Cryst. Growth 220 (2000) 494.
[25] H.Q. Le, S.K. Lim, G.K.L. Goh, S.J. Chua, J.X. Ong, J. Electrochem. Soc. 157 (2010) H796.
[26] K.Y. Cheong, N. Muti, S.R. Ramanan, Thin Solid Films 410 (2002) 142.
[27] N.H. Nickel, F. Friedrich, J.F. Rommeluère, P. Galtier, Appl. Phys. Lett. 87 (2005) 211905.
[28] G.K.L. Goh, C.G. Levi, J.H. Choi, F.F. Lange, J. Cryst. Growth 286 (2006) 457.
[29] JCPDS Card No. 36–1451.
[30] JCPDS Card No. 41–1103.
[31] J.D. Ye, S.L. Gu, S.M. Zhu, S.M. Liu, Y.D. Zheng, R. Zhang, Y. Shi, H.Q. Yu, Y.D. Ye, J. Cryst. Growth 283 (2005) 279.
[32] A.R. Babar, P.R. Deshamukh, R.J. Deokate, D. Haranath, C.H. Bhosale, K.Y. Rajpure, J. Phys. D: Appl. Phys. 41 (2008) 135404.
[33] C. Giacovazzo, H.L. Monaco, G. Artioli, D. Viterbo, G. Ferraris, G. Gilli, G. Zanotti, M. Catti, Fundamentals of Crystallography, International Union of Crystallography, Oxford Science Publications, USA, 2002.
[34] R.T. Sanderson, J. Am. Chem. Soc. 105 (1983) 2259.
[35] W.-J. Li, E.-W. Shi, W.-Z. Zhong, Z.-W. Yin, J. Cryst. Growth 203 (1999) 186.
[36] R.W. Nosker, P. Mark, J.D. Levine, Surf. Sci. 19 (1970) 291.
[37] L.E. Greene, M. Law, D.H. Tan, M. Montano, J. Goldberger, G. Somorjai, P. Yang, Nano Lett. 5 (2005) 1231.
[38] G. Cao, Nanostructures and Nanomaterials: Synthesis, Properties and Applications, first ed., Imperial College Press, London, 2004.
[39] M. Lucas, Z.L. Wang, E. Riedo, Phys. Rev. B 81 (2010) 045415.
[40] X. Gao, X. Li, W. Yu, J. Phys. Chem. B 109 (2005) 1155.
[41] J.J. Richardson, F.F. Lange, Cryst. Growth Des. 9 (2009) 2570.
[42] F. Li, L. Hu, Z. Li, X. Huang, J. Alloys Compd. 465 (2008) L14.
[43] U.N. Maiti, S. Nandy, S. Karan, B. Mallik, K.K. Chattopadhyay, Appl. Surf. Sci. 254 (2008) 7266.
[44] W. Peng, Sh. Qu, G. Cong, Zh. Wang, Cryst. Growth Des. 6 (2006) 1518.
[45] A. Degen, M. Kosec, J. Eur. Ceram. Soc. 20 (2000) 667.
[46] X. Feng, L. Feng, M. Jin, J. Zhai, L. Jiang, D. Zhu, J. Am. Chem. Soc. 126 (2004) 62.
[47] A.Y.L. Sim, G.K.L. Goh, S. Tripathy, D. Andeen, F.F. Lange, Electrochim. Acta 52 (2007) 2933.
[48] D.A. Schwartz, N.S. Norberg, Q.P. Nguyen, J.M. Parker, D.R. Gamelin, J. Am. Chem. Soc. 125 (2003) 13205.

[49] J.D. Bryan, D.A. Schwartz, D.R. Gamelin, J. Nanosci. Nanotechnol. 5 (2005) 1472.
[50] C.A. Arguello, D.L. Rousseau, S.P.S. Porto, Phys. Rev. 181 (1969) 1351.
[51] H.K. Yadav, K. Sreenivas, R.S. Katiyar, V. Gupta, J. Phys. D: Appl. Phys. 40 (2007) 6005.
[52] T.C. Damen, S.P.S. Porto, B. Tell, Phys. Rev. 142 (1966) 570.
[53] J.M. Calleja, M. Cardona, Phys. Rev. B 16 (1977) 3753.
[54] X. Wang, J. Xu, X. Yu, K. Xue, J. Yu, X. Zhao, Appl. Phys. Lett. 91 (2007) 031908.
[55] A. Kaschner, H. Siegle, G. Kaczmarczyk, M. Straßburg, A. Hoffmann, C. Thomsen, U. Birkle, S. Einfeldt, D. Hommel, Appl. Phys. Lett. 74 (1999) 3281.
[56] Y.H. Gao, Y. Bando, T. Sato, Y.F. Zhang, X.Q. Gao, Appl. Phys. Lett. 81 (2002) 2267.
[57] H.J. Chun, Y.S. Choi, S.Y. Bae, H.W. Seo, S.J. Hong, J. Park, H. Yang, J. Phys. Chem. B 107 (2003) 9042.
[58] R. Rao, A.M. Rao, B. Xu, J. Dong, S. Sharma, M.K. Sunkara, J. Appl. Phys. 98 (2005) 094312.